Aeroacoustic Analysis of a Counter Rotating Open Rotor based on the Harmonic Balance Method

Daniel Lindblad *, Gonzalo Montero Villar †, Niklas Andersson ‡ and Alexandre Capitao Patrao §
Chalmers University of Technology, Gothenburg, SE-412 96, Sweden

Suk-kee Courty-Audren ¶ and Gaël Napias ‖
ISAE-SUPAERO, Université de Toulouse, Toulouse, 31400, France

The Counter Rotating Open Rotor (CROR) powerplant is an interesting architecture for future regional aircraft propulsion since it offers higher propulsive efficiency and thereby lower fuel consumption than the conventional Turbofan engine. The noise levels generated are however potentially larger compared to a Turbofan due in part to the absence of a ducting nacelle. This raises the need for efficient, high fidelity tools that can be used for the design and evaluation of new blade concepts capable of meeting strict noise regulations. In this paper, a Computational Aeroacoustics (CAA) platform for CRORs based on the Harmonic Balance method is presented. The method is formulated in the time domain and solves for the dominant frequencies of the flow by expressing the solution as a truncated Fourier series in time. Coupling between the resolved frequencies is furthermore possible since the nonlinear URANS equations are solved for. The far field acoustic signature is obtained by solving a convective form of the Ffowcs Williams-Hawkings equations for permeable surfaces. The CAA platform is applied to a generic, full scale, pusher type CROR operating at cruise conditions.

I. Nomenclature

Roman/Greek

D	=	time spectral derivative matrix, s^{-1}
$\mathcal{F}_j$	=	vector containing total flux
$\mathcal{F}_j^*$	=	vector containing total flux for all time levels
$\mathcal{H}$	=	vector containing source terms
$\mathcal{H}^*$	=	vector containing source terms for all time levels
L_{ij}	=	modified stress tensor, Pa
N	=	number of blades in blade row
N_h	=	number of harmonics
N_t	=	number of time levels
Q_i	=	modified momentum tensor, kg m^{-2} s^{-1}
Q	=	vector containing conserved variables
Q^*	=	vector containing conserved variables for all time levels
$\hat{Q}_n$	=	Fourier coefficient vector for n^{th} harmonic
$\hat{Q}_{n,k}$	=	time-azimuthal Fourier coefficient vector
S	=	phase shift matrix
t, τ	=	time, s
T	=	time period, s
x, r, θ	=	cylindrical coordinates
x_1, x_2, x_3	=	Cartesian coordinates

*Ph.D. Student, Department of Mechanics and Maritime Sciences, Hörsalsvägen 7A, SE-412 96 Gothenburg.
†Ph.D. Student, Department of Mechanics and Maritime Sciences, Hörsalsvägen 7A, SE-412 96 Gothenburg.
‡Assistant Professor, Department of Mechanics and Maritime Sciences, Hörsalsvägen 7A, SE-412 96 Gothenburg.
§Ph.D. Student, Department of Mechanics and Maritime Sciences, Hörsalsvägen 7A, SE-412 96 Gothenburg.
¶Ph.D., Department of Aerodynamics, Energetics and Propulsion, 10 avenue Édouard Belin, 54032 Toulouse.
‖Research Engineer, Department of Aerodynamics, Energetics and Propulsion, 10 avenue Édouard Belin, 54032 Toulouse.

β = phase lag, rad
ω_n = angular frequency of n^{th} harmonic, rad s^{-1}
Ω = rotational speed of blade row, rad s^{-1}

Subscripts

0 = free stream property
b = index of blade row (1=first rotor, 2=second rotor)

II. Introduction

The noise generated by a Counter Rotating Open Rotor (CROR) can be divided into tonal and broadband components. The tonal noise is emitted at discrete frequencies that are integer multiples of the blade passing frequencies (BPF) of each blade row [1], and is commonly subdivided into self and interaction noise. Self noise is linked to the volume displacement and steady loading of the rotor blades [2]. Interaction noise is on the other hand generated due to the unsteady loading of the blades caused by interaction between the two, counter rotating, blade rows. In contrast to tonal noise, broadband noise is emitted across a broad frequency spectrum and is related to turbulence. A more extensive review of the noise sources of a CROR can be found in e.g. [3].

Several numerical methods are available today for predicting the noise generated by a CROR. A common approach used by several authors is to couple high fidelity computational fluid dynamics (CFD) simulations in the near field around the CROR with an acoustic analogy, commonly based on the Ffowcs Williams-Hawkings (FW-H) equation [4], in order to compute the far field acoustic signature. Although CFD has the capability of predicting all the aforementioned noise sources, the analysis is often restricted to the tonal components by solving the URANS equations. This choice is not immediately justified, given that broadband noise may be an important contributor to the overall noise levels of a CROR [5]. For a CROR however, limited computational resources often prevent broadband noise from being accounted for by CFD based methods due to the high computational cost associated with scale resolving simulations. It can also be argued that since the tonal sources are deterministic in nature, they are more easily targeted for acoustic optimization by tailoring the shape of the blades. Within the URANS framework, both linearized and nonlinear methods exist. The former alternative is based on linearizing the equations about a steady mean flow and then solving for the amplitude of the decoupled, unsteady perturbations. This method is computationally fast, accurate, and well established for predicting turbofan noise [6, 7]. It has also been applied successfully to CRORs by e.g. Sharma et al. [2]. If coupling between the unsteady perturbations is to be accounted for, the nonlinear terms in the URANS equations must be retained in the analysis. A common approach in this case is to integrate the equations in time [8–10], possibly in combination with the Chorochronic method [11] which is used to reduce the computational domain to one blade per row. Although time accurate solutions generally are computationally expensive, this approach has the clear advantage of making few assumptions on the nature of the flow apart from the choice of turbulence modeling. Another alternative for simulating the unsteady flow field around a CROR is the Harmonic Balance method proposed by Hall et al. [12]. This approach places somewhere in between linearized and time accurate methods in the sense that it retains the nonlinear terms of the URANS equations, but only solves for a selected number, contrary to all the frequencies that constitutes the unsteady solution. Both the Harmonic Balance method as well as similar methods have been employed for turbomachinery tonal noise predictions with good results, see e.g. [9, 13–15] .

Although the Harmonic Balance method has shown promising results for turbomachinery aeroacoustics problems, it has not yet been extensively applied to CRORs. The purpose of the present paper is therefore to explore this application further by developing a complete tonal noise prediction framework in which the Harmonic Balance method is used to simulate the unsteady flow around the rotors. The far field noise signature is obtained by coupling the Harmonic Balance solution with a FW-H methodology for permeable sampling surfaces [16]. In order to evaluate the framework, a full-scale CROR operating at cruise conditions is considered. The unsteady flow field predicted by the Harmonic Balance method is analyzed and related to the far field acoustic signature obtained with the FW-H methodology. Some problems, especially with regards to how the acoustic integration surface is placed, are also identified and discussed.

III. Computational Framework

A. Flow Solver

The computational framework presented in this paper for predicting CROR tonal noise has been implemented into Chalmers' in-house CFD solver G3D::Flow. G3D::Flow is a massively parallel code for simulating both compressible and incompressible flows using a range of turbulence models. In this work, the Favre-averaged Navier-Stokes equations coupled with the low-Reynolds number $k-\varepsilon$ turbulence model by Chien [17] are used to model the flow around the rotors. The governing equations may in compact form be written as

$$\frac{\partial \mathcal{Q}}{\partial t} + \frac{\partial \mathcal{F}_j}{\partial x_j} = \mathcal{H} \tag{1}$$

In this equation, $\mathcal{Q}$ is the state vector containing the conserved variables, $\mathcal{F}_j$ is the total flux vector and $\mathcal{H}$ is the source vector that contains the turbulence model source terms. The equations are discretized on a boundary-fitted, non-orthogonal, curvilinear, multi-block mesh using the finite volume technique. Convective fluxes are reconstructed on cell faces using a third-order upwind scheme that determines the direction of upwinding based on 1D characteristic analysis. Diffusive fluxes are calculated on cell faces by a second-order centered difference scheme. In order to advance the equations in time, a three-stage, second order accurate Runge-Kutta method is employed. In cases where a steady solution is sought, the time step is furthermore adapted locally in each cell according to the CFL criterion.

B. Harmonic Balance Method

The Harmonic Balance form of the governing equations (Eq. (1)) are derived by assuming that the conserved variables present in the state vector $\mathcal{Q}$ are periodic in time [12]. This assumption allows the solution to be expressed as a temporal Fourier series with spatially varying coefficients

$$\mathcal{Q}(t, \mathbf{x}) = \sum_{n=-\infty}^{\infty} \hat{\mathcal{Q}}_n(\mathbf{x}) e^{i\omega_{n,b} t} \tag{2}$$

It is assumed that the only source of unsteadiness withing the blade rows of the CROR is the periodic passing of the adjacent blade row. This implies that the angular frequency of the n^{th} harmonic in each relative frame of reference may be computed as [14]

$$\begin{aligned} \omega_{n,1} &= nN_2(\Omega_2 - \Omega_1) \\ \omega_{n,2} &= nN_1(\Omega_1 - \Omega_2) \end{aligned} \tag{3}$$

Here, N_b and Ω_b respectively denote the number of blades and the rotational speed of blade row $b = 1, 2$. The time period of the unsteadiness is furthermore given by

$$\begin{aligned} T_1 &= \frac{2\pi}{N_2|\Omega_2 - \Omega_1|} \\ T_2 &= \frac{2\pi}{N_1|\Omega_1 - \Omega_2|} \end{aligned} \tag{4}$$

The Fourier series representation in Eq. (2) is now approximated by assuming that a limited number of harmonics is sufficient to accurately describe the periodic nature of the flow

$$\mathcal{Q}(t) \approx \sum_{n=-N_h}^{N_h} \hat{\mathcal{Q}}_n e^{i\omega_{n,b} t} \tag{5}$$

Note that the spatial dependency of the Fourier coefficients was omitted here for brevity. In the Harmonic Balance method the solution is computed at $N_t = 2N_h + 1$ time instances, also called time levels, equally distributed over the time period. A new state vector $\mathcal{Q}^*$ is therefore introduced to contain the solution at each time level

$$\mathcal{Q}^* = \left[\, \mathcal{Q}_0, \, \mathcal{Q}_1, \, \ldots, \, \mathcal{Q}_{N_t - 1} \, \right]^T \tag{6}$$

Note that in this equation, $\mathcal{Q}_l = \mathcal{Q}(t_{l,b})$, where $t_{l,b} = lT_b/N_t$ is the time at time level l. A coupled set of mathematically steady state equations can be formulated for the solution at each time level by treating the time derivative of $\mathcal{Q}_m$ as

a source term. In order to do this, we start by calculating the Fourier coefficients in Eq. (5) from a discrete Fourier transform over all stored time levels

$$\hat{Q}_n = \frac{1}{N_t} \sum_{l=0}^{N_t-1} Q_l \; e^{-i\omega_{n,b} t_{l,b}} \tag{7}$$

The time derivative of Q_m can now be computed by differentiating Eq. (5) with respect to time, combining the resulting expression with Eq. (7) and setting $t = t_{m,b}$

$$\frac{\partial Q_m}{\partial t} \approx \sum_{n=-N_h}^{N_h} i\omega_{n,b} \left(\frac{1}{N_t} \sum_{l=0}^{N_t-1} Q_l \; e^{-i\omega_{n,b} t_{l,b}} \right) e^{i\omega_{n,b} t_{m,b}} \tag{8}$$

Interchanging the order or summation and combining the exponential terms further yields

$$\frac{\partial Q_m}{\partial t} \approx \sum_{l=0}^{N_t-1} \left(\frac{i}{N_t} \sum_{n=-N_h}^{N_h} \omega_{n,b} e^{i\omega_{n,b}(t_{m,b}-t_{l,b})} \right) Q_l \tag{9}$$

With this equation we have obtained a high order finite difference approximation of the time derivative, based on a stencil that spans over all stored time levels. Equation (9) may also be expressed as a matrix multiplication according to

$$\frac{\partial Q^*}{\partial t} \approx D_b Q^* \tag{10}$$

In this equation, D_b is known as the time spectral derivative matrix for bladerow b and is block structured into $N_t \times N_t$ blocks. Each block contains a diagonal matrix of size $N_{var} \times N_{var}$, where N_{var} is the number of conserved variables present in Q. The entries of the diagonal matrix in block (m, l) are all equal and will here be denoted $d^b_{m,l}$. A compact analytical expression for these elements may be obtained by evaluating the summation within the parenthesis of Eq. (9), for a complete derivation see [18]

$$d^b_{m,l} = \begin{cases} 0, & l = m \\ \frac{\pi}{T_b} (-1)^{(m-l)} \csc\left(\frac{\pi(m-l)}{N_t}\right), & l \neq m \end{cases} \tag{11}$$

The governing equation for the new state vector may now be formulated as follows

$$D_b Q^* + \frac{\partial \mathcal{F}^*_j}{\partial x_j} = \mathcal{H}^* \tag{12}$$

The new flux and source vectors respectively contain the total flux and source terms at each time level

$$\begin{aligned} \mathcal{F}^*_j &= \left[\; \mathcal{F}_{j,0}, \; \mathcal{F}_{j,1}, \; \ldots, \; \mathcal{F}_{j,N_t-1} \; \right]^T \\ \mathcal{H}^* &= \left[\; \mathcal{H}_0, \; \mathcal{H}_1, \; \ldots, \; \mathcal{H}_{N_t-1} \; \right]^T \end{aligned} \tag{13}$$

The Harmonic Balance solver starts by looping through all time levels and adds the flux and turbulent source terms to the discretized flow residual. After this, the time spectral derivative is added to the flow residual and the solution is finally advanced in pseudo time until convergence is reached.

C. Phase-Shifted Periodic Boundary Conditions

Phase-shifted periodic boundary conditions are used to enable the two rotors of the CROR to interact in the general case when $N_1 \neq N_2$ and the computational domain is reduced to contain only one blade per row. A derivation of the equations necessary for phase-shifting the Harmonic Balance solution at the periodic interface is presented here in cylindrical coordinates. To begin with, it is observed that the solution in one blade passage must be equal to the flow in an adjacent blade passage at a different time $t + \Delta t_b$. This may be expressed as

$$Q(x, r, \theta + \zeta\theta_{S,b}, t) = Q(x, r, \theta, t + \Delta t_b) \tag{14}$$

Here, $\theta_{S,b} = 2\pi/N_b > 0$ and $\zeta = \pm 1$ is used to indicate whether the conserved variables are shifted in the positive or negative θ direction. The time shift can be computed as $\Delta t_b = \zeta \beta_b T_b / 2\pi$, where β_b is the phase lag between two adjacent blade passages [11]

$$\beta_b = -2\pi \ \text{sign}(\Omega_1 - \Omega_2) \frac{N_1 - N_2}{N_b} \tag{15}$$

Equation (5) is now combined with Eq. (14) to obtain

$$\sum_{n=-N_h}^{N_h} \hat{\boldsymbol{Q}}_n(x, r, \theta + \zeta\theta_{S,b}) e^{i\omega_{n,b}t} = \sum_{n=-N_h}^{N_h} \hat{\boldsymbol{Q}}_n(x, r, \theta) e^{i\omega_{n,b}(t+\Delta t_b)} \tag{16}$$

From the orthogonality of the Fourier basis we further get

$$\hat{\boldsymbol{Q}}_n(x, r, \theta + \zeta\theta_{S,b}) = \hat{\boldsymbol{Q}}_n(x, r, \theta) e^{i\omega_{n,b}\Delta t_b} \tag{17}$$

By inserting Eq. (17) into Eq. (5) and evaluating the resulting expression at time level m, the following equation for the phase shifted solution is obtained

$$\boldsymbol{Q}_m(x, r, \theta + \zeta\theta_{S,b}) = \sum_{n=-N_h}^{N_h} \left[\left(\frac{1}{N_t} \sum_{l=0}^{N_t-1} \boldsymbol{Q}_l(x, r, \theta) e^{-i\omega_{n,b}t_{l,b}} \right) e^{i\omega_{n,b}\Delta t_b} \right] e^{i\omega_{n,b}t_{m,b}} \tag{18}$$

The order of summation in Eq. (18) can finally be rearranged to obtain a matrix relation between $\boldsymbol{Q}^*(\theta)$ and $\boldsymbol{Q}^*(\theta + \zeta\theta_{S,b})$

$$\boldsymbol{Q}^*(\theta + \zeta\theta_{S,b}) = S_b \boldsymbol{Q}^*(\theta) \tag{19}$$

The matrix S_b has the same structure as D_b and the elements of the diagonal matrix in block (m, l) can be shown to be given by [19]

$$s^b_{m,l} = \frac{1}{N_t} \left(1 + 2 \sum_{n=1}^{N_h} \cos\left(\left[\frac{2\pi(m-l)}{N_t} + \zeta\beta_b \right] n \right) \right) \tag{20}$$

In the special case when $N_1 = N_2$, $\beta_b = 0$ according to Eq. (15). In this case, it is found that Eq. (20) yields the identity matrix, and thus a normal periodic boundary condition is obtained.

D. Fourier Based Rotor-Rotor Interface

The blade row interface implemented into G3D::Flow is based on the theory presented by Olausson [14]. This theory is in turn similar to the technique developed by Gerolymos et al. [11] for the Chorochronic method. The interface works by sampling the flow into time-azimuthal Fourier coefficients on both sides of the interface and then uses these coefficients to transfer information between the blade rows. For the case when the problem consists of a single pair of blade rows in relative motion, such as a CROR, the flow is circumferentially periodic with azimuthal mode numbers on the form [20, 21]

$$m_{n,k} = kN_1 + nN_2 \tag{21}$$

In order to distinguish the frequency with which these modes propagate in the relative frame attached to the first and second blade row, we change the indices in Eq. (3) according to

$$\begin{aligned} \omega_{n,1} &= nN_2(\Omega_2 - \Omega_1) \\ \omega_{k,2} &= kN_1(\Omega_1 - \Omega_2) \end{aligned} \tag{22}$$

Note that both n and k may take on any integer value (positive or negative). The time-azimuthal periodicity implies that the Fourier representation in Eq. (5) may be generalized as follows for the first and second blade row respectively

$$
\begin{aligned}
Q(x,r,\theta,t) &= \sum_{n=-N_h}^{N_h} \sum_{k=-N_h}^{N_h} \hat{Q}_{n,k}(x,r) e^{i(\omega_{n,1} t - m_{n,k}\theta)} \\
Q(x,r,\theta,t) &= \sum_{n=-N_h}^{N_h} \sum_{k=-N_h}^{N_h} \hat{Q}_{n,k}(x,r) e^{i(\omega_{k,2} t - m_{n,k}\theta)}
\end{aligned}
\tag{23}
$$

The time-azimuthal Fourier coefficients ($\hat{Q}_{n,k}$) can be calculated on both sides of the interface by integrating the corresponding temporal Fourier coefficients in the circumferential direction according to

$$
\begin{aligned}
\hat{Q}_{n,k}(x,r) &= \frac{N_1}{2\pi} \int_0^{2\pi/N_1} \hat{Q}_n(x,r,\theta) e^{i m_{n,k}\theta} \mathrm{d}\theta \\
\hat{Q}_{n,k}(x,r) &= \frac{N_2}{2\pi} \int_0^{2\pi/N_2} \hat{Q}_k(x,r,\theta) e^{i m_{n,k}\theta} \mathrm{d}\theta
\end{aligned}
\tag{24}
$$

The temporal Fourier coefficients ($\hat{Q}_{n/k}$) are furthermore obtained by employing Eq. (7) on the conserved variables, converted to cylindrical coordinates and the absolute frame of reference. Information transfer between the blade rows is finally achieved by using the time-azimuthal Fourier coefficients obtained on one side of the interface to calculate ghost cell values at the corresponding radial location on the other side of the interface according to Eq. (23).

A note should be made with regards to the choice of N_h as a limit for the series expansion in Eq. (23). For the Harmonic Balance method, it is natural to choose the upper bound on n and k to N_h when evaluating the first and second expression in Eq. (23) respectively. This is because N_h represents the largest number of temporal harmonics that are solved for in the Harmonic Balance computation. To motivate the choice of the other summation limit in Eq. (23), we must turn to Eq. (24). We note that the time-azimithal Fourier coefficient obtained from the second expression in Eq. (24) will be used in the first expression of Eq. (23) for calculating ghost cell values in the first blade row, and vice versa for the second. Accordingly, since only N_h temporal harmonics are resolved in each bladerow, the largest value of k in the second expression of Eq. (24) must be N_h. This explains why the other summation limit must be chosen to N_h as well.

E. Ffowcs Williams-Hawkings Formulation

The goal of the present work is to calculate the tonal noise generated by a CROR in flight for a set of far field observers that are fixed relative to the engine. This is sometimes referred to as the wind-tunnel problem, since it is equivalent to calculating the noise generated by a stationary engine at a set of fixed observers inside a wind tunnel. We adopt the convention that the free stream velocity around the CROR is $U_0 > 0$ in the positive x_1 direction, implying that the engine is flying at a speed U_0 in the negative x_1 direction. The noise levels are obtained as the solution to a convective form of the Ffowcs Williams-Hawkings (FW-H) equation for permeable surfaces proposed by Najafi-Yazdi et al. [16]. The advantage of their Formulation 1C is that it explicitly accounts for the effects of the free stream velocity on the sound radiation, making it directly applicable for wind-tunnel problems. The solution to the permeable FW-H equation expresses the far field pressure signal as a surface integral over a closed surface Γ, plus an integral taken over the volume exterior to the surface [16]. The integration surface does not need to represent a physical surface and flow is thus allowed to cross it, which is why it is often called permeable. As discussed by di Francescantonio [22], the surface integral over a permeable surface will account for all mono- di- and quadropole noise sources enclosed by the surface. Noise generation as well as nonlinear effects on noise propagation in the volume exterior to the surface is in turn accounted for by the volume integral. The volume integral is omitted for the far field noise predictions presented in this work, which implies that the integration surface must be chosen large enough to encapsulate all the relevant nonlinearities of the problem. Since data on the integration surface is obtained from a CFD simulation, the surface must also be placed such that restrictions on the CFD mesh resolution necessary for noise generation and propagation can be met inside it [23, 24].

For a stationary integration surface that does not move relative to the observer, Formulation 1C of Najafi-Yazdi et al. [16] may be expressed as follows

$$
\begin{aligned}
4\pi p'(\mathbf{x},t) = &\int_\Gamma \left[\frac{R\dot{Q}_i n_i}{R^{*2}} - U_0 \frac{\tilde{R}_1^* Q_i n_i}{R^{*2}} \right]_{\text{ret}} \mathrm{d}\Gamma \\
&+ \int_\Gamma \left[\frac{1}{c_0} \frac{\dot{L}_{ij} n_j \tilde{R}_i}{R^*} + \frac{L_{ij} n_j \tilde{R}_i^*}{R^{*2}} \right]_{\text{ret}} \mathrm{d}\Gamma
\end{aligned}
\tag{25}
$$

where the modified momentum and stress tensors are defined respectively as

$$
\begin{aligned}
Q_i &= \rho(u_i + U_{0i}) - \rho_0 U_{0i} \\
L_{ij} &= \rho u_i (u_j + U_{0j}) + (p - p_0)\delta_{ij} - \tau_{ij}
\end{aligned}
\tag{26}
$$

In Eqs. (25) and (26), subscript 0 denotes free stream properties. The velocity vector u_i is the perturbation velocity in an inertial frame of reference attached to the engine. The absolute velocity obtained from the CFD simulation is consequently given by $u_i + U_{0i}$. It is assumed that the viscous stress tensor (τ_{ij}) in Eq. (26) is negligible and it is consequently omitted in the evaluation of L_{ij}. The additional variables in Eq. (25) are furthermore defined as

$$
\begin{aligned}
R &= \frac{-M_0(x_1 - y_1) + R^*}{\beta^2} \\
R^* &= \sqrt{(x_1 - y_1)^2 + \beta^2 \left[(x_2 - y_2)^2 + (x_3 - y_3)^2 \right]} \\
\beta &= \sqrt{1 - M_0^2} \\
\tilde{R}_1 &= \frac{1}{\beta^2}(-M_0 + \tilde{R}_1^*),\ \tilde{R}_2 = \frac{x_2 - y_2}{R^*},\ \tilde{R}_3 = \frac{x_3 - y_3}{R^*} \\
\tilde{R}_1^* &= \frac{x_1 - y_1}{R^*},\ \tilde{R}_2^* = \beta^2 \frac{x_2 - y_2}{R^*},\ \tilde{R}_3^* = \beta^2 \frac{x_3 - y_3}{R^*}
\end{aligned}
\tag{27}
$$

Here, $\mathbf{x}$ and $\mathbf{y}$ respectively denote the observer location and the point on Γ where the integrand is being evaluated and $M_0 = U_0/c_0$ is the free stream Mach number. As indicated in Eq. (25), the integrand must be evaluated at a retarded time τ, representing the time when an acoustic signal generated at $\mathbf{y}$ reaches the observer at position $\mathbf{x}$ and time t. In the presence of a mean flow, the equation for τ takes on the following form

$$
\tau = t - \frac{R}{c_0} \tag{28}
$$

It should also be noted that a dot above a quantity in Eq. (25) represents time differentiation with respect to the retarded time. In the special case when $U_0 = 0$, the above equations reduce to the "Second KFWH Equation" for stationary, permeable surfaces presented by di Francescantonio [22]. Formulation 1C has been implemented as a source time dominant algorithm [25], other names include forward time and advanced time algorithm.

A similar approach to the one presented in [2] is used to transfer data from the rotating frame of reference used in the CFD computations onto the inertial integration surface used in Eq. (25). To begin with, the Harmonic Balance solution (Q^*) is extracted on surfaces in front and above the forward rotor as well as above and behind the rear rotor. Since only one blade passage is used in the CFD simulations, the extracted surfaces have to be rotated and phase shifted (using Eq. (19)) in order to obtain a complete solution that covers the full circumference. As the FW-H solver iterates in source time, this solution is used to calculate $Q(\tau_i)$ by combining Eq. (7) with Eq. (5). The conserved variables at time τ_i are then converted to the absolute frame of reference and rotated to the correct physical position according to the rotational speed of each respective blade row. Finally, the conserved variables are converted to primitive variables, the free stream velocity is subtracted and the result is interpolated onto the surface Γ.

IV. Computational Setup

A. Geometry and Meshing

The CROR geometry used for this paper was designed using the in-house propeller design tool OPTOPROP developed at Chalmers [26]. This design tool employs a Blade Element-Momentum method for designing the propeller blades, akin to the methodology published by Adkins et al. [27], that has been extended to allow for the design of a

CROR. The extended methodology accounts both for non-uniform inflow to the rotors and for the rotors' mutual effect on each other, making it suitable for designing an entire CROR. The design features 12 forward and 10 rear blades, with the forward rotor having a diameter of 4.2672 m. The rear rotor diameter is clipped by 15%, with the aim of reducing the interaction noise due to the impingement of the front rotor tip vortex on the rear rotor.

The blade design obtained with OPTOPROP was validated by performing steady CFD simulations under cruise conditions at $M_0 = 0.75$, which was also chosen as the operating point for the aeroacoustic analysis. It was found that the thrust obtained in CFD matched well with the thrust target set in OPTOPROP, but also that the rear blade was very highly loaded. It was therefore decided to reduce the rotational speed of the rear rotor by 20% in order to improve its aerodynamic performance. As a consequence of this choice, the thrust and torque split for the final design used in the aeroacoustic analysis were not entirely representative for powering a regional aircraft. The final design parameters of the CROR are summarized in Table 1.

Table 1 CROR design parameters.

Blade configuration	12x10
D_1	4.2672m
D_2	3.6271m
Hub to tip ratio (forward rotor)	0.35
Rotor-rotor spacing	$0.27D_1$
Ω_2/Ω_1	0.8
Airfoil	NACA16

IGG™ and AutoGrid5™ v10.2 of the NUMECA FINE™/Turbo software were used to discretize the computational domain into a multi-block structured mesh. An example of the mesh and schematic view of the computational domain are presented in Fig. 1 and Fig. 2 respectively. Above the main channel containing the rotors, the domain extends radially to a total height equal to four times the front rotor radius. As shown in Fig. 2, the domains is also split into two counter rotating sub domains and is characterized by a total size of about 47M cells. O-grid and H-grid blocks were used around the blades and in the blade passage respectively. The number cells in the radial direction were set to 157 in the main channel and 153 in the far field. Different sizes were chosen for the first cell at wall: 5 μm on the blade surface and 1 mm on the hub surface. In the azimuthal direction, the number of points were set to 165 in the first rotor domain and 161 for the second rotor. This was done in order to ensure that azimuthal mode numbers with $k = 3$ and $n = 5$ are resolved with 20 points per wavelength, c.f. Eq. (21). The blade surfaces were discretized with 353 cells around the circumference of the blade. Extra care was also put towards keeping the maximum expansion ratio below 1.1 in the main channel.

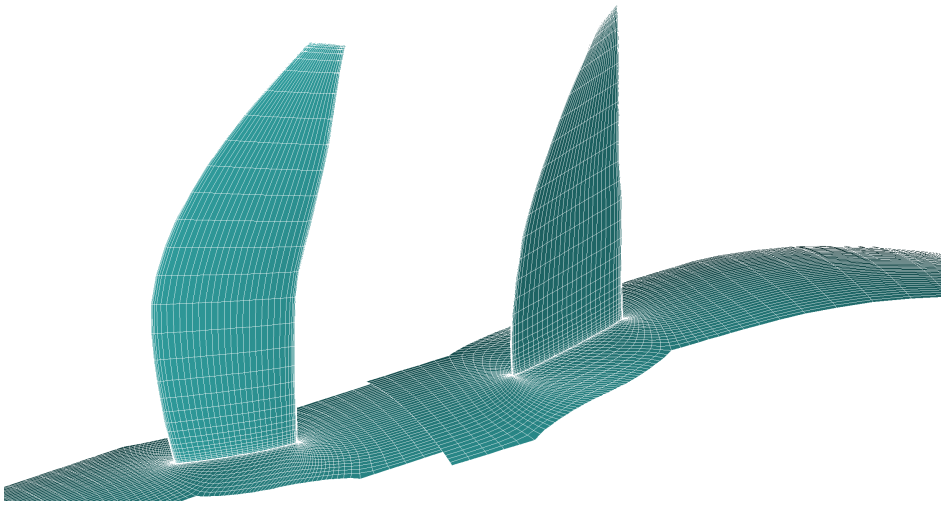

Fig. 1 3D view of solid mesh (every other node shown).

B. Simulation Settings

A schematic view of the computational domain, including the different boundary conditions employed, is presented in Fig. 2. As can be seen from this figure, the two counter rotating domains are connected with the rotor-rotor interface described in section III.D. For simplicity, the entire nacelle of the CROR and the fictitious hub included upstream and downstream of the nacelle are modeled as non-viscous (slip) walls. Free stream properties are prescribed at the inlet and far field boundary using a 1D absorbing boundary condition and a constant static pressure is set at the outlet.

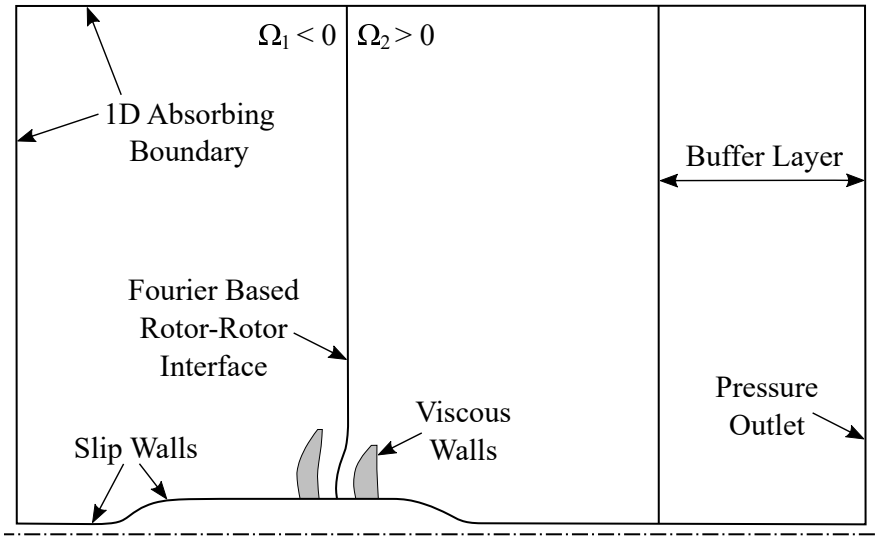

Fig. 2 Schematic view of the computational domain, including the boundary conditions employed.

The aeroacoustic analysis was split up into three stages. First, a steady simulation was performed in which the thrust on both rotors was stabilized to vary less than 1%. After this, a Harmonic Balance simulation with $N_h = 3$ harmonics was restarted from the converged steady state solution. The thrust on both rotors was once again monitored in order to assess the convergence of the simulation. In particular, the thrust on the rear rotor was checked for each individual time level in order to see the influence that the front rotor wake has on the rear rotor thrust. The simulation was stopped when the thrust on the rear rotor had stabilized for all time levels. In the final step, the converged Harmonic Balance solution was post processed using the FW-H methodology presented in section III.E. The far field acoustic signature was calculated at a set of observer positions located on a line parallel to the engine axis, $10D_1$ to the side of the CROR as illustrated in Fig. 3.

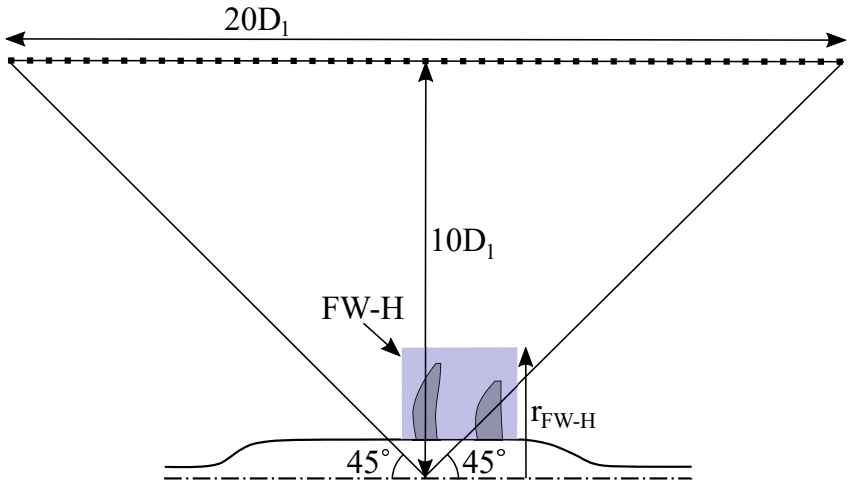

Fig. 3 Schematic view of far field observer locations and FW-H integration surface.

As shown in e.g. [1, 2], the deterministic flow field within the blade rows of a CROR generates frequencies on the form $\omega_{l,m} = lN_1\Omega_1 + mN_2\Omega_2$ in the absolute frame of reference. These frequencies are sometimes referred to as the sum and difference tones, since they are integer multiples of the blade passing frequencies ($BPF_b = N_b\Omega_b$) of the two blade rows. Based on the data presented in Table 1, the lowest frequency and thereby the time period of the flow in the absolute frame of reference was determined. Sampling at the observers was done at a rate of 340 samples per period and continued until pressure data for 5 complete periods had been obtained for all observers. The integration surface was located about one blade chord upstream and downstream of the leading and trailing edge of the front and read rotor respectively. The radius of the integration surface was furthermore chosen to $r_{\text{FW-H}} = 1.05D_1$ and the mesh resolution was set to $\Delta x \approx 0.01$m.

Two additional methods are used to improve the accuracy and convergence of the Harmonic Balance simulation. First, temporal damping is added to the Harmonic Balance equations in a buffer layer upstream of the outlet (see Fig. 2) according to the methodology described in [15]. This is done in order to prevent transient waves from reflecting against the non-absorbing outlet boundary and degrade the quality of the solution. Secondly, the time spectral viscosity operator proposed by Huang et al. [28] is added to the turbulence equations (k and ε). The time spectral viscosity operator works by damping the amplitude of the unsteady harmonics, and in the limit of infinite damping it drives the solution towards the mean value. A large viscosity coefficient is used in this work, which effectively means that the turbulence variables are frozen in the Harmonic Balance computations. The motivation for doing this is that the turbulence quantities were found to become negative when blade row interactions causes the wakes to flap. The reason to why this problem is localized to the flapping wake region is that the spatial gradients of k and ε are very large here. Consequently, when the wake flaps the variations of these quantities in a cell can become very large between different time levels. This may cause the time spectral derivative source term to go negative, which after some solver iterations gives negative turbulent quantities. Time spectral viscosity was found to efficiently limit oscillations in turbulent quantities due to the wake flapping motion, which further prevented unphysical, negative turbulent quantities in this region. No time spectral viscosity is added to the mass, momentum and energy equations.

V. Results

A. Validation of FW-H Formulation

The implementation of Formulation 1C by Najafi-Yazidi et al. [16] that is used in this work has been validated for a mono- and dipole situated in uniform mean flows of varying Mach numbers. This was done by comparing numerical predictions of RMS pressure to the analytical solution at a set of observer locations situated on a half circle with center at the sound source. Comparisons for the monopole were done at a distance of $r = 340$m and for the dipole at a distance of $r = 30$m. The analytical solutions for the velocity, pressure and density fluctuations generated by a mono- and dipole may be expressed in terms of potential functions. For a monopole situated at the origin, the function takes on the following form [16]

$$\phi_{\text{Mono}}(\mathbf{x}, t) = \frac{A}{4\pi R^*} e^{i\omega\left(t - \frac{R}{c_0}\right)} \tag{29}$$

The potential function for a dipole aligned with the x_2 axis is furthermore obtained as

$$\phi_{\text{Dipo}}(\mathbf{x}, t) = \frac{\partial}{\partial x_2}\phi_{\text{Mono}}(\mathbf{x}, t) \tag{30}$$

When the mean flow is in the positive x_1 direction, the velocity, pressure and density fluctuations at a point $\mathbf{x}$ can be expressed as

$$\begin{aligned} u_i(\mathbf{x}, t) &= \frac{\partial}{\partial x_i}\phi(\mathbf{x}, t) \\ p'(\mathbf{x}, t) &= -\rho_0\left(\frac{\partial}{\partial t} + U_0\frac{\partial}{\partial x_1}\right)\phi(\mathbf{x}, t) \\ \rho'(\mathbf{x}, t) &= \frac{p'(\mathbf{x}, t)}{c_0^2} \end{aligned} \tag{31}$$

The numerical solutions were obtained by evaluating the integral in Eq. (25) on a stationary surface enclosing the sound source. The integration surface was chosen to be a cylinder with both a height and radius of 1m, and all flow

properties necessary to evaluate Eq. (25) were obtained directly at the surface from the expressions in Eq. (31). The amplitude, frequency, density and speed of sound in Eqs. (29)-(31) were respectively set to A= 1 $m^3 s^{-1}$, $\omega = 10\pi$ rad s^{-1}, $\rho_0 = 1$ kg m^{-3}, and $c_0 = 340$m s^{-1}.

Validation results for the monopole are presented in terms of polar directivity plots for two freestream Mach numbers in Fig. 4. Agreement between analytical and numerical predictions can be seen to be excellent across all polar directivities for both the $M_0 = 0.5$ and $M_0 = 0.85$ case. As expected, the uniform noise radiation of the monopole is altered by the free stream flow, resulting in higher noise levels upstream of the source.

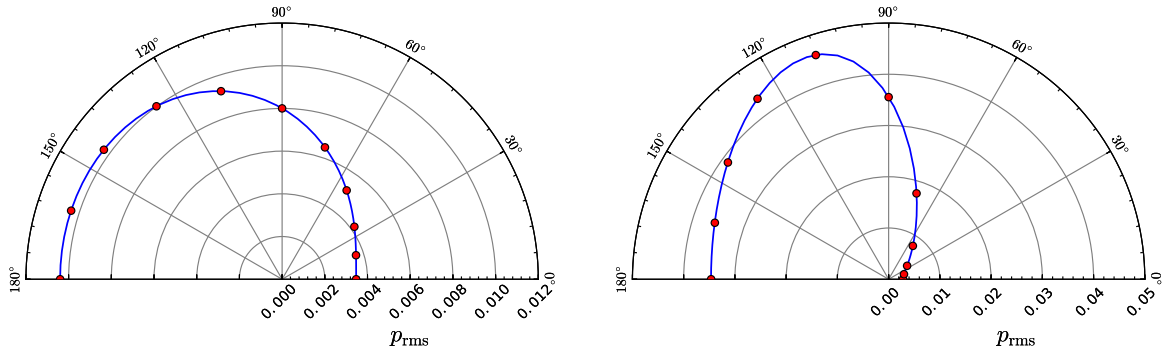

(a) $M_0 = 0.5$. **(b) $M_0 = 0.85$.**

Fig. 4 Comparison of polar directivity for a monopole at a distance r=340m. The analytical solutions are represented by solid blue lines and results from the FW-H methodology by red markers.

Polar directivity plots obtained for the dipole are presented in Fig. 5. The analytical and numerical predictions of the far field noise signature can be seen to agree very well for the dipole source too. The effects of the free stream are also clearly visible by the fact that noise radiation is stronger in the upstream direction. It should be noted that our settings for the lower Mach number cases ($M_0 = 0.5$) were chosen to match the ones that Najafi-Yazidi et al. [16] used for validating their implementation of Formulation 1C. When compared, the results presented in Fig. 4a and 5a appear to agree very well with those presented in [16].

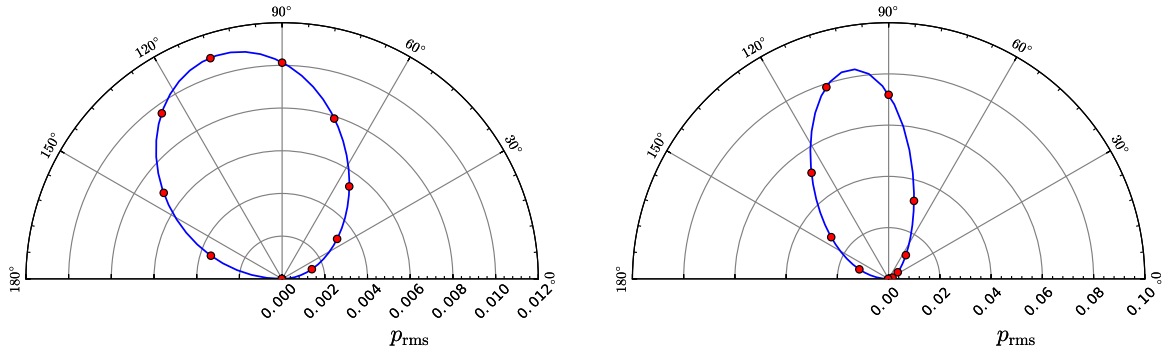

(a) $M_0 = 0.5$. **(b) $M_0 = 0.85$.**

Fig. 5 Comparison of polar directivity for a dipole at a distance r=30m. The analytical solutions are represented by solid blue lines and results from the FW-H methodology by red markers.

Based on the presented validation it can be concluded that the FW-H formulation used in this paper gives correct far field noise signatures for both mono- and dipole noise source across the range of free stream Mach numbers relevant for a CROR in cruise. As noted in section III.E, quadrupole noise can also be accounted for by Formulation 1C. This case remains to be validated in order to fully cover all relevant noise source mechanisms encountered in a CROR. It should also be emphasized that the interpolation routines used to transfer flow field data from the CFD simulation on to the integration surface are not covered by the current validation.

B. Unsteady Flowfield Analysis

The unsteady flow field obtained from the Harmonic Balance solver with $N_h = 3$ harmonics will in this section be analyzed in some detail. The aim is to gain some understanding of the noise generation mechanisms before moving on to the far field noise results presented in the next section. To begin with, entropy contours at midspan of the CROR are presented in Fig. 6. Two things are worth noting in this figure. Firstly, the Fourier based rotor-rotor interface can be seen to filter out some of the azimuthal harmonics of the first rotor wake as it passes over the interface. This is expected, since the limited number of harmonics retained in the Harmonic Balance analysis requires that a limited number of wake harmonics are transferred from the first to the second blade row, c.f. section III.D. Secondly, it is noted that the the first rotor wake has been phase shifted over the periodic boundary in the second blade row. This indicates that the phase shifted periodic boundary conditions are working as intended.

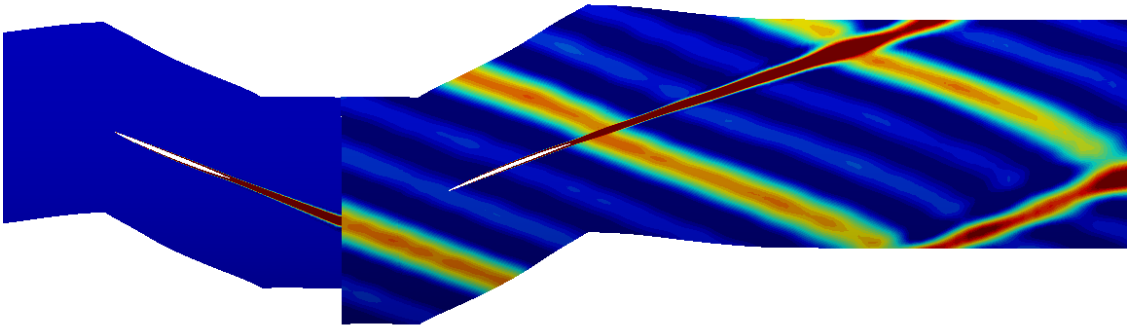

Fig. 6 Entropy contours at midspan of the CROR.

The analysis is continued by studying the pressure field on a set of planes with normals along the engine axis. To begin with, static pressure on two planes located upstream of the rotor-rotor interface are shown in Fig. 7. From Fig. 7a the pressure field swept by the first rotor is clearly visible. In particular, the shock attached to the trailing edge of the first rotor can be identified as a sharp tangential gradient in the pressure field. It is notable that this shock extends quite far radially above the rotor, implying that nonlinear effects which are important for noise generation/propagation could be significant quite far away from the engine for this case. Moving on to Fig. 7b, the shock is once again clearly visible from the sharp pressure gradients seen in the field. The low pressure of the tip vortex core is also visible behind the tip of the rotors. Another notable feature in Fig. 7b is that no effects of the rear rotor are visible, at least not with the chosen scale.

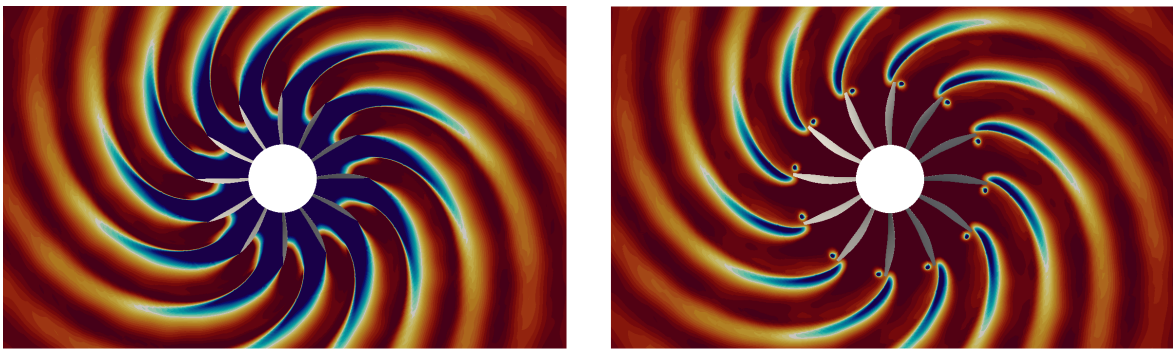

(a) Plane through pitch axis of first rotor. **(b) Plane behind first rotor.**

Fig. 7 Pressure field upstream of rotor-rotor interface. The single-passage solution has been phase-shifted and rotated to cover the whole circumference. Scale spans 1 kPa.

The static pressure at two planes located downstream of the rotor-rotor interface are shown in Fig. 8. Turning first to Fig. 8a, depicting a plane in front of the rear rotor, it can be noted that the concentrated tip vortex seen in Fig. 7b has been filtered out slightly over the rotor-rotor interface. Some spurious oscillations can also be observed between the tip vortices. These oscillations are likely due to the limited number of harmonics used in the Harmonic Balance solver, as

discussed in relation to the entropy contours in Fig. 6. Moving on to Fig. 8b, where the plane is located at the pitch axis of the second rotor, it is noted that the spurious oscillations around the tip vortex are stronger. This may be due to interaction effects between the tip vortex and the flow field generated by the rear rotor. Another notable feature in Fig. 8b is that the pressure field swept by the rear rotor is considerably weaker than the corresponding field swept by the forward rotor. This illustrates the uneven torque split of this CROR mentioned in section IV.A.

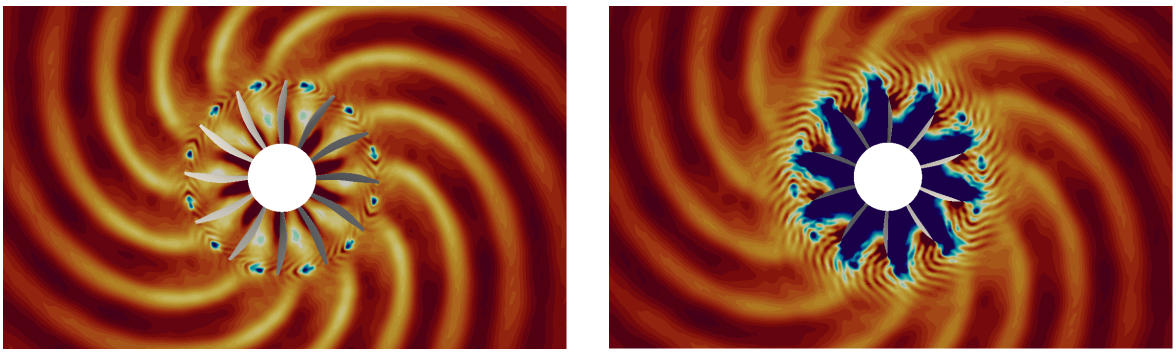

(a) Plane before second rotor. **(b) Plane through pitch axis of second rotor.**

Fig. 8 Pressure field downstream of rotor-rotor interface. The single-passage solution has been phase-shifted and rotated to cover the whole circumference. Scale spans 1 kPa.

C. Farfield Noise Signature

The farfield noise signature of the CROR is illustrated in terms of Sound Pressure Level (SPL) directivity plots for some selected frequencies in Fig. 9. Frequencies that are multiples of an individual blade passing frequency have been isolated in Fig. 9a. The noise generated by the individual blade rows, sometimes referred to as self noise, will be generated at these frequencies. From Fig. 9a, it is evident that the blade passing frequency of the first blade row dominates the noise signature around the axial location where the rotors are situated. Another interesting feature seen in this figure is that the self noise generated by the second blade row is considerably lower in amplitude. These results are in line with the observation made earlier that the pressure field swept by the front rotor is considerably stronger than that of the rear rotor (see Fig. 7 and 8). It can also be noted that the individual blade passing frequency directivity plots in Fig. 9a have similar shapes to those obtained by other authors [10, 13].

The directivity of some selected frequencies that are multiples of both blade passing frequencies are illustrated in Fig. 9b. These frequencies are typically generated due to interaction between the two blade rows [1], and the origin of the noise is therefore also harder to establish. If it is assumed that the noise originates from the impingement of the front rotor wake on the second blade row, then the frequencies presented in Fig. 9b represent noise due to scattering of the first wake harmonic [2]. In general, it is observed that the interaction noise presented in Fig. 9b shows a more complicated directivity pattern compared to the self noise in Fig. 9a. Another interesting feature of the interaction noise is that it is not only concentrated to the center where the rotors are situated. In fact, the interaction noise is stronger than the self noise both in the far upstream and downstream directions. A note should also be made with regards to the frequency denoted $BPF_1 + 3BPF_2$ in Fig. 9b. This frequency can be seen to have its peak amplitude around the plane of the rotors, which is typical for self noise. Considering that the same frequency also corresponds to $3BPF_1$, it is therefore believed that both self noise and interaction noise contribute to the amplitude of this frequency.

Further analysis of Fig. 9 reveals that the total SPL directivity exhibit spurious oscillations in the downstream direction. In order to investigate the cause of this, the noise spectra at one observer located approximately 27m downstream of the front rotor pitch axis is illustrated in Fig. 10a. As can be seen from this figure, the spectra contains a considerable amount of frequencies above $30BPF_1$. These frequencies are believed to be unphysical and contribute to the oscillations seen in the total SPL directivity. The oscillations were found to disappear when the signal was low pass filtered to remove all frequencies above $10BPF_1$. This confirms that higher frequencies are responsible for the oscillations seen in the total SPL directivity, but gives little information regarding the root of the problem. In order to get more information, the surface behind the rear rotor was excluded when performing the FW-H integral. The noise spectra obtained for the same observer without the downstream surface included is presented in Fig. 10b. From this figure it is evident that the higher frequencies have disappeared. The total SPL directivity was also found to not

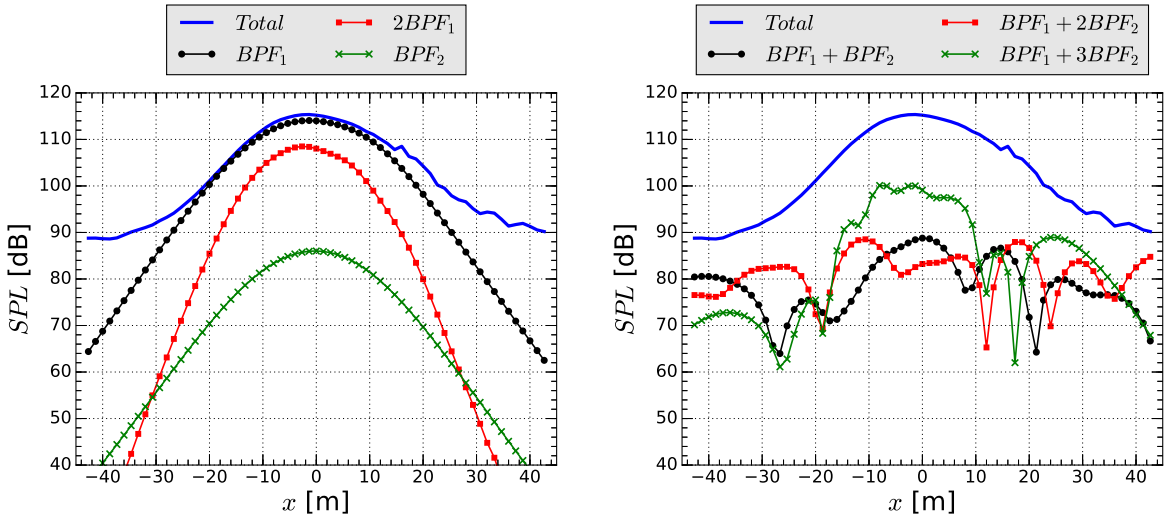

(a) Multiples of an individual blade passing frequency. **(b) Multiples of both blade passing frequencies.**

Fig. 9 Noise directivity for some selected frequencies and the total sound pressure level of the CROR.

contain any spurious oscillations once the downstream surface was excluded. It is therefore concluded that the root of the spurious oscillations stems from high frequency (above $10BPF_1$) signals on the surface behind the rear rotor. One possible cause of these signals is the rear rotor wake and tip vortex crossing the integration surface. As explained by Farassat [24], when the exterior volume integral is excluded in the far field acoustic analysis, wakes crossing the integration surface may generate a spurious signal. Although this hypothesis can not be proven with the available data, it seems plausible due to the high harmonics content found in the sharp wake of a CROR blade.

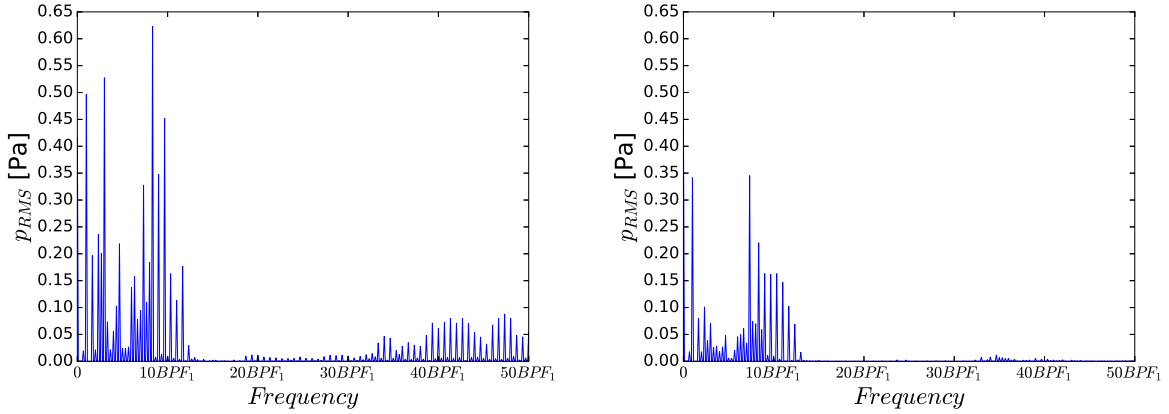

(a) Noise spectra obtained with the downstream surface. **(b) Spectra obtained without the downstream surface.**

Fig. 10 Comparison of noise spectra obtained 27m downstream of the front rotor pitch axis with and without the surface behind the rear rotor included in the FW-H integral.

VI. Conclusions

In the present paper, a computational framework for predicting the tonal noise generated by a CROR has been presented. The framework uses high fidelity, unsteady CFD computations based on the nonlinear Harmonic Balance method [12] to define the noise source. The Harmonic Balance method is used in combination with phase shifted periodic boundary conditions to reduce the computational domain to one blade per row and blade row coupling is furthermore realized by transferring time-azimuthal Fourier coefficients across the rotor-rotor interface. The converged

CFD computation is finally used as input to a Ffowcs Williams-Hawkings (FW-H) methodology based on Formulation 1C by Najafi-Yazidi et al. [16] to compute the far field noise signature of the CROR.

The proposed framework was applied to a full scale CROR operating at cruise conditions. The unsteady flow field predicted in the CFD computations was analyzed and related to the far field noise signature obtained by the FW-H methodology. It was found that the self noise of the front rotor dominated the noise signature at most observer locations, which could be related to the uneven torque split between the front and rear rotor that characterizes the investigated CROR geometry. More detailed analysis of the noise signature revealed that spurious oscillations were present in the total SPL levels at some downstream directivities. This problem turned out to originate from the FW-H integration surface placed downstream of the rear rotor. It is hypothesized that the root of the problem is the wake of the rear rotor crossing the integration surface, which may generate a spurious signal at the observer when the volume integral is excluded from the FW-H analysis [24]. Another source of uncertainty in the far field noise prediction is that the shock attached to the front rotor extends outside of the chosen integration surface. This will to some extent affect the results, since nonlinearities exterior to the surface are excluded from the analysis. A larger integration surface, both in the downstream and radial direction, could potentially alleviate the two aforementioned problems. For the present study, however, the CFD mesh was primarily generated to support accurate noise propagation in the vicinity of the blades. Increasing the size of the integration surface would thus require a more computationally expensive CFD mesh, which was deemed out of scope for the present study.

The present study focused on investigating the CROR under cruise conditions. Although this allowed for the complete framework to be demonstrated and tested, it is recognized that it is more relevant to study take-off and approach conditions since certification targets must be met at these operating points. Applying the present methodology at take-off and approach is is however straightforward, although it should be kept in mind that e.g. blade separation may complicate the analysis. It also remains to fully validate the proposed framework at the relevant operating points. To this date, the Harmonic Balance solver has been validated for a set of turbomachinery tonal noise problems in [15] and the implemented FW-H methodology was validated within this study.

Acknowledgments

This work is financially supported by the E.U. under the ULTIMATE * Project funded by the European Commission within the Horizon 2020 Programme (2014-2020) under the Grant Agreement No 633436. The authors would also like to acknowledge the Swedish National Infrastructure for Computing (SNIC) for providing computer resources at the National Supercomputing Centre (NSC) in Linköping, Sweden and Chalmers Centre for Computational Science and Engineering (C^3SE) in Gothenburg, Sweden.

References

[1] Hanson, D. B., "Noise of Counter-rotation Propellers," *Journal of Aircraft*, Vol. 22, No. 7, 1985, pp. 609–617.

[2] Sharma, A., and Chen, H., "Prediction of aerodynamic tonal noise from open rotors," *Journal of Sound and Vibration*, Vol. 332, No. 16, 2013, pp. 3832–3845.

[3] Peake, N., and Parry, A. B., "Modern Challenges Facing Turbomachinery Aeroacoustics," *Annual Review of Fluid Mechanics*, Vol. 44, No. 1, 2012, pp. 227–248.

[4] Ffowcs Williams, J. E., and Hawkings, D. L., "Sound Generation by Turbulence and Surfaces in Arbitrary Motion," *Philosophical Transactions of the Royal Society of London. Series A, Mathematics and Physical Sciences*, Vol. 264, No. 1151, 1969, pp. 321–342.

[5] Parry, A. B., Kingan, M., and Tester, B. J., "Relative importance of open rotor tone and broadband noise sources," *17th AIAA/CEAS Aeroacoustics Conference*, AIAA Paper 2011-2763, 2011.

[6] Envia, E., Wilson, A. G., and Huff, D. L., "Fan Noise: A Challenge to CAA," *International Journal of Computational Fluid Dynamics*, Vol. 18, No. 6, 2004, pp. 471–480.

[7] Frey, C., Ashcroft, G., Kersken, H.-P., and Weckmüller, C., "Advanced Numerical Methods for the Prediction of Tonal Noise in Turbomachinery — Part II: Time-Linearized Methods," *Journal of Turbomachinery*, Vol. 136, No. 2, 2014, pp. 021003–1–021003–10.

*Ultra Low emission Technology Innovations for Mid-century Aircraft Turbine Engines

[8] Colin, Y., Blanc, F., Caruelle, B., Barrois, F., and Djordjevic, N., "Computational stratedy for predicting CROR noise at low-speed Part II: Investigation of the Noise Sources Computation with the Chorochronic Approach," *18th AIAA/CEAS Aeroacoustics Conference*, AIAA Paper 2012-2222, 2012.

[9] Hoffner, P.-A., Deconinck, T., Hirsch, C., Pascal, S., Ortun, B., Canard-Caruana, S., Rahier, G., and Caruelle, B., "Aeroacoustic Computations of Contra-Rotating Open Rotors using the Nonlinear Harmonic Method and a Chorochronic Approach," *ASME Turbo Expo 2012: Turbine Technical Conference and Exposition*, GT2012-68982, 2012.

[10] Stuermer, A., and Yin, J., "Low-Speed Aerodynamics and Aeroacoustics of CROR Propulsion Systems," *15th AIAA/CEAS Aeroacoustics Conference*, AIAA Paper 2009-3134, 2009.

[11] Gerolymos, G. A., Michon, G. J., and Neubauer, J., "Analysis and Application of Chorochronic Periodicity in Turbomachinery Rotor/Stator Interaction Computations," *Journal of Propulsion and Power*, Vol. 18, No. 6, 2002, pp. 1139–1152.

[12] Hall, K. C., Jeffrey, P. T., and Clark, W. S., "Computation of Unsteady Nonlinear Flows in Cascades Using a Harmonic Balance Technique," *AIAA Journal*, Vol. 40, No. 5, 2002, pp. 879–886.

[13] Van Zante, D. E., and Envia, E., "Prediction of the Aero-Acoustic Performance of Open Rotors," *ASME Turbo Expo 2014: Turbine Technical Conference and Exposition*, GT2014-26413, 2014.

[14] Olausson, M., "Turbomachinery Aeroacoustic Calculations using Nonlinear Methods," Ph.D. thesis, Division of Fluid Dynamics, Department of Applied Mechanics, Chalmers University of Technology, Gothenburg, 2011.

[15] Lindblad, D., and Andersson, N., "Validating the Harmonic Balance Method for Turbomachinery Tonal Noise Predictions," *55th AIAA Aerospace Sciences Meeting*, AIAA Paper 2017-1171, 2017.

[16] Najafi-Yazidi, A., Brès, G. A., and Mongeau, L., "An Acoustic Analogy Formulation for Moving Sources in Uniformly Moving Media," *Proceedings of the Royal Society A, Mathematical, Physical and Engineering Sciences*, Vol. 467, No. 2125, 2011, pp. 144–165.

[17] Chien, K.-Y., "Predictions of Channel and Boundary-Layer Flows with a Low-Reynolds-Number Turbulence Model," *AIAA Journal*, Vol. 20, No. 1, 1982, pp. 33–38.

[18] Gopinath, A. K., and Jameson, A., "Application of the Time Spectral Method to Periodic Unsteady Vortex Shedding," *44th AIAA Aerospace Sciences Meeting and Exhibit*, AIAA Paper 2006-0449, 2006.

[19] Sicot, F., Dufour, G., and Gourdain, N., "A Time-Domain Harmonic Balance Method for Rotor/Stator Interactions," *Journal of Turbomachinery*, Vol. 134, No. 1, 2012, pp. 011001–1–011001–13.

[20] Tyler, J. M., and Sofrin, T. G., "Axial Flow Compressor Noise Studies," *SAE Technical Paper*, 620532, 1962.

[21] Ekici, K., and Hall, K. C., "Nonlinear Analysis of Unsteady Flows in Multistage Turbomachines Using Harmonic Balance," *AIAA Journal*, Vol. 45, No. 5, 2007, pp. 1047–1057.

[22] di Francescantonio, P., "A New Boundary Integral Formulation for the Prediction of Sound Radiation," *Journal of Sound and Vibration*, Vol. 202, No. 4, 1997, pp. 491–509.

[23] Farassat, F., "Derivation of Formulations 1 and 1A of Farassat," Technical Report NASA/TM-2007-214853, NASA, Hampton, VA, March 2007.

[24] Farassat, F., "Open Rotor Noise Prediction at NASA Langley - Capabilities, Research and Development," Technical Report NASA/TM-2010-216178, NASA, Hampton, VA, January 2010.

[25] Brentner, K. S., and Farassat, F., "Modeling aerodynamically generated sound of helicopter rotors," *Progress in Aerospace Sciences*, Vol. 39, No. 2-3, 2003, pp. 83–120.

[26] Capitao Patrao, A., "Implementation of Blade Element Momentum/Vortex Methods for the Design of Aero Engine Propellers," Research report - Department of Mechanics and Maritime Sciences 2017:06, Chalmers University of Technology, Gothenburg, November 2017.

[27] Adkins, C. N., and Liebeck, R. H., "Design of Optimum Propellers," *Journal of Propulsion and Power*, Vol. 10, No. 5, 1994, pp. 676–682.

[28] Huang, H., and Ekici, K., "Stabilization of High-Dimensional Harmonic Balance Solvers Using Time Spectral Viscosity," *AIAA Journal*, Vol. 52, No. 8, 2014, pp. 1784–1794.